Research Square

Preprints are preliminary reports that have not undergone peer review.
They should not be considered conclusive, used to inform clinical practice,
or referenced by the media as validated information.

HPV-driven DNA methylation plasticity reshapes immune regulation in head and neck cancer

Felipe Luz Torres Silva
State University of Campinas (UNICAMP)
Fatemeh Farshadi
McGill University
Marco Mascarella
Segal Cancer Centre of the Lady Davis Institute for Medical Research, McGill University
Alex Mlynarek
Segal Cancer Centre of the Lady Davis Institute for Medical Research, McGill University
Moulay A. Alaoui-Jamali
McGill University
Michael Hier
Segal Cancer Centre of the Lady Davis Institute for Medical Research, McGill University
Mariana Maschietto
State University of Campinas (UNICAMP)
Sabrina Daniela Silva Wurzba
sabrina.wurzba@mcgill.ca

McGill University

Article

Keywords: Head and neck squamous cell carcinoma, Human papillomavirus, Epigenetic reprogramming, DNA methylation, Tumor immune microenvironment, Immune spatial organization, T-cell regulation, Fibroblast–immune interactions, Single-cell imaging mass cytometry

Posted Date: November 12th, 2026

DOI: https://doi.org/10.21203/rs.3.rs-11476184/v1

License: This work is licensed under a Creative Commons Attribution 4.0 International License.
Read Full License

Additional Declarations: No competing interests reported.

HPV-driven DNA methylation plasticity reshapes immune regulation in head and neck cancer

Felipe Luz Torres Silva[1,2], Fatemeh Farshadi[3,4], Marco Mascarella[4,5], Alex Mlynarek[4,5], Moulay A. Alaoui-Jamali[3,4], Michael Hier[4,5], Mariana Maschietto[1,6†], Sabrina Daniela da Silva Wurzba[3,4,5†*]

1. Postgraduate Program in Genetics and Molecular Biology, Institute of Biology, State University of Campinas (UNICAMP), Campinas, São Paulo, Brazil.

2. Department of Genetics, Institute of Biological Sciences, Federal University of Amazonas (UFAM), Manaus, Amazonas, Brazil.

3. Division of Experimental Medicine, Department of Medicine and Health Sciences, McGill University, Montreal, QC, Canada.

4. Segal Cancer Centre of the Lady Davis Institute for Medical Research, Sir Mortimer B. Davis-Jewish General Hospital, McGill University, Montreal, QC, Canada.

5. Department of Otolaryngology-Head and Neck Surgery, McGill University, Montreal, QC, Canada.

6. Research Center, Boldrini Children's Center, Campinas, Sao Paulo, Brazil

† Equal senior contributors

* Correspondence: Sabrina Wurzba, PhD, MSc, DDS

Head and Neck Cancer Translational Research Laboratory for Advancing Learning (HEAL-HNC); Department of Otolaryngology-Head and Neck Surgery, Faculty of Medicine, McGill University. Montreal, QC H3T 1E2 – Canada. Phone: (514) 340-8222.

E-mail: sabrina.wurzba@mcgill.ca

Translational Relevance

This study investigates DNA methylation signatures impacting the tumor microenvironment (TME) of head and neck cancer (HNC) associated with specific risk factors. By integrating advanced high-throughput platforms, including Human Methylation 450K BeadChip microarrays and single-cell imaging mass cytometry (IMC), we identified distinct methylation signatures and immune landscapes in HNC associated with HPV-positive *versus* HPV-negative tumors. Differentially methylated *loci* were significantly enriched in immune regulatory pathways, with particularly strong signatures related to T-lymphocyte regulation. Further spatially resolved analysis of immunological components within the tumor microenvironment revealed that, in HPV-positive tumors, T lymphocytes exhibit intrinsic self-regulatory activity. In contrast, in HPV-negative tumors, this regulatory program is attenuated and appears to be modulated through fibroblast-mediated interactions, with fibroblasts emerging as the predominant cellular partners of T lymphocytes in this setting. This epigenetically regulated spatial cellular dynamic within the tumor microenvironment provides a framework for more precise clinical decision-making and the development of personalized therapeutic strategies for patients with HNC.

Abstract

The incidence of HPV-related HNC has exponentially increased over recent decades in head and neck cancer (HNC). Although HPV infection is known to reprogram the host epigenetic landscape, the cellular and functional consequences of HPV-mediated DNA methylation changes remain poorly defined. Here we demonstrated that HPV-driven epigenetic reprogramming reshapes immune regulation within the HNC tumor microenvironment (TME), generating distinct methylation landscapes associated with viral status. Genome-wide methylation analysis identified differentially methylated loci enriched in immune-related pathways, supporting a central role for epigenetic remodeling in shaping HPV-specific tumor–immune interactions. To link epigenetic differences to cellular organization and function within the TME, we characterized immune and stromal compartments, cell–cell interactions, and spatial architecture using high-dimensional single-cell imaging mass cytometry (IMC). Key findings were independently validated in an external single-cell RNA sequencing cohort. We identified 770 differentially methylated positions ($P<0.05$, $|logFC| <0.20$) mapping to 386 genes that distinguish HPV-positive from HPV-negative tumors, with significant enrichment in immune-related pathways. Single-cell high-dimension IMC revealed distinct immune architectures between tumor types. In HPV-negative tumors, immune exclusion was primarily associated with fibroblast-dominated spatial organization that physically and functionally insulated tumor cells from immune surveillance. In contrast, T cells in HPV-positive tumors exhibited an intrinsic autocrine regulatory program characterized by robust type I and type II interferon signaling, consistent with enhanced tumor recognition and immune engagement. These findings demonstrate that HPV-associated DNA methylation reprogramming shapes the spatial and functional organization of the TME in HNC, promoting divergent mechanisms of immune regulation and tumor immune evasion.

Keywords: Head and neck squamous cell carcinoma; Human papillomavirus; Epigenetic reprogramming; DNA methylation; Tumor immune microenvironment; Immune spatial

organization; T-cell regulation; Fibroblast–immune interactions; Single-cell imaging mass cytometry.

Introduction

Head and neck cancer (HNC) is the 6th most common cancer worldwide presenting 890.000 new cases and 450.000 deaths per year [1]. The actual incidence is expected to rise 30% by the year 2030 due to the exponential increase in human papillomavirus (HPV) infection [2]. Patients with HNC receive treatment based on surgery, radiotherapy, chemotherapy, immunotherapy, or combinations of these modalities [3]. These approaches fail to account for inter- and intra-tumor heterogeneity that can directly impact the therapeutic response [4]. Despite substantial advances in surgical techniques and pharmacotherapy, the clinical outcomes for patients with advanced disease remain poor, with 5-year survival rates stagnant at <50% [5]. Molecular and epidemiological studies consistently identified tobacco use, alcohol consumption, and HPV infection as major risk factors driving somatic mutations, epigenetic dysregulation that ultimately promote HNC development [6,7]. However, despite well-established epidemiological links between these exposures and disease risk, the HPV-associated epigenetic alterations underlying HNC progression remain incompletely characterized [8–10].

DNA methylation has a central role in the regulation of gene expression and maintenance of genomic stability. Distinct cancer types exhibit characteristic DNA methylation landscapes that are associated with clinical outcomes and disease progression [11,12]. These epigenetic alterations are associated with key etiological risk factors and can modulate tumor immunogenicity, as well as the composition and function of immune cell populations critical for effective anti-tumor responses [13,14]. The tumor microenvironment (TME) is a major determinant of HNC progression, a concept underscored by the clinical success of immune checkpoint inhibitors [15,16]. The TME comprises a complex and dynamic network of immune cells, mesenchymal stromal cells, and extracellular matrix components that interact with tumor cells to influence tumor growth, metastatic dissemination, and therapeutic response [17-19]. Despite its recognized importance, a comprehensive spatial and functional characterization of the HNC TME in the context of HPV infection remains limited. In this study, we characterize DNA

methylation profiles in HNC patient samples to determine how HPV-associated epigenetic alterations shape the tumor microenvironment.

Materials and methods

Study population

Frozen tumor specimens from primary HNC patients were obtained at the time of surgical resection at an academic medical centre (Jewish General Hospital, Montreal, Canada). The cohort included patients with established high-risk etiological factors HPV infection, tobacco use, and alcohol consumption, with longitudinal follow-up of up to 157 months (>10 years). DNA methylation profiling was performed on frozen tumor samples, while single-cell imaging mass cytometry (IMC) analyses were conducted using archival formalin-fixed, paraffin-embedded (FFPE) tissue blocks. Representative hematoxylin and eosin (H&E)-stained sections were reviewed for histopathological confirmation. All FFPE samples were independently evaluated by two board-certified pathologists to confirm tumor content and select regions for analysis. Patients were followed up after treatment for routine surveillance, and any tumor relapse was histologically confirmed. Eligible participants were previously untreated patients without evidence of distant metastasis (M0), undergoing curative-intent surgical resection, and treated at a single tertiary-care center. Tumors were re-staged according to the current International Union Against Cancer (UICC) TNM classification and grouped as early-stage (T1–2N0) or advanced-stage disease (T3–4N0-3 or T1-2N1-3). Detailed clinicopathological data were extracted from medical records (**Supplemental Tables 1 and 2**). Both female and male participants were included in this study. Sex was considered in the study design, and the findings are intended to be relevant to both sexes. All patients provided written informed consent, and tissue collection and analysis were conducted in accordance with the Declaration of Helsinki. The study protocol was approved by the institutional research ethics board (#CR17-44). Reporting adhered to the Strengthening the

Reporting of Observational Studies in Epidemiology (STROBE) guidelines to ensure methodological rigor. DNA methylation profiling using the Illumina HumanMethylation450 BeadChip was performed on 21 tumor samples, while IMC analysis was conducted on 20 samples (**Figure 1**).

Bisulfite treatment and DNA methylation profiling

Genomic DNA was extracted from tumor tissue using DNeasy Blood & Tissue Kit (Qiagen) following the manufacturer's instructions. DNA from frozen tissues was converted using the EZ DNA Methylation kit (Zymo Research, USA) according to the manufacturer's recommendations. Bisulfite-converted DNA was hybridized in the Human Methylation 450 BeadChip microarrays (HM450K, Illumina, USA), following the Illumina Infinium HD methylation protocol, followed by images acquisition by the Illumina iScan SQ scanner (Illumina, USA). The fluorescence signals were interpreted with the GenomeStudio software (v.2011.1 with the methylation module v.1.9.0; Illumina, USA). Probes were annotated according to the Illumina annotation file using UCSC version hg19 of the human reference genome.

Copy number alteration (CNA) analysis

The 450k methylation array data were subjected to copy-number variation (CNV) analysis using the Conumee2 R package [20]. Each probed CpG is typically represented by two probes on the array (one for methylated and one for unmethylated). The methylation and unmethylated signal intensities are combined for the computation of CNV, and a ratio is created against healthy reference samples with a flat genome. The location of each chromosome is then used to plot this copy-number ratio on a graph. For normalization, a set of 71 control samples with a balanced copy-number profile from both male and female donors

were used. Conumee2 CNV.summaryplot() function was used to plot the CNA percentages across samples.

Differentially methylated probes and immune deconvolution analysis

Minfi R package [21] was used to examine IDAT files, and the functional normalization (FunNorm) method [22] was used to normalize them. 428,062 probes remained for additional analysis after XYS and low-quality probes were eliminated. For unsupervised non-linear dimension reduction based on standard deviation, the 10,000 most variable probes were employed. Using pheatmap (version 1.0.12) using the Ward method and euclidean for the distance matrix, heatmaps and hierarchical clustering were carried out. Tumor immune cell infiltration and tumor cell purity were estimated using normalized B-values and the MethylResolver R package 0.1.0. It compares the B-values of bulk tissues to the methylation signature taken from 11 different types of leukocyte cells using a deconvolution technique [23].

Imaging mass cytometry (IMC) and data acquisition

IMC was performed in anonymized FFPE samples from 20 HNC patients using Fluidigm Hyperion Imaging Mass Cytometer System (IMC™, Fluidigm, USA) for laser-based cell ablation and imaging following the manufacturer's instructions (**Figure 1**). The system had a 1μm resolution and gathered channel-specific signal data on a per-pixel basis. This data helped record signal localization (corresponding to nuclear, cytoplasmic, and membrane) and intensity per individual cells. Cellular regions were identified by correlating with Ir191/193 which labels DNA, and CD45, e-cadherin, Pan-CK, smooth muscle actin (SMA) and vimentin for the cytoplasmic. A panel with 20 metal-conjugated antibodies to interrogate the proteins of interest in the TME of HNC including the target, clone information and metal isotype tag, is available in the **Supplemental Table 3**. Conjugations of the metal to the antibodies were done using the Maxpar labeling kit (Fluidigm, USA). The concentration of the antibodies was adjusted by titration, ranging from 100 to 500 μg ml−1, using Nanodrop (Thermo Scientific,

USA). FFPE sections were prepared, stained with the designed antibody panel as previously described [24]. Laser ablation was performed on the regions of interest at a frequency of 200Hz, resulting in a pixel size/resolution of 1 μm2. The raw data underwent preprocessing using the CyTOF software v7.0 (Fluidigm, USA).

IMC data preprocessing and analysis

The images were analyzed following the protocol as previously published [25]. The first step includes quality control by manually reviewing the raw data using plugins such as napari-imc [26] and ImageJ [27] for IMC. The steinbock toolkit was used for multi-channel image processing, including multi-channel image segmentation, object quantification and data export. The outputs from stainbock pipeline were used as input for imcRtools and cytomapper R/Bioconductor packages to read spatially resolved, single-cell and images as described [25]. IMC data were processed from Steinbock pipeline outputs, generating a SpatialExperimentobject containing per-cell marker intensities, spatial coordinates, and neighborhood graphs. Marker intensities were transformed using an arcsinh transformation (cofactor = 5). Quality control included inspection of signal distributions per marker and per cell, with removal of channels showing low variability or signal close to background, as well as exclusion of cells with extremely low total signal (outliers in the lower tail of the total intensity distribution).

Sample integration was performed using Seurat method, applying standard normalization (NormalizeData) and identification of variable features (FindVariableFeatures). Dimensionality reduction was carried out by principal component analysis (PCA) using the first 20–30 principal components, followed by Seurat-based integration to mitigate inter-sample effects. UMAP embeddings were computed from the selected PCs for visualization.

Cell clustering was performed by constructing a shared nearest-neighbor graph (FindNeighbors) followed by community detection (FindClusters) using a resolution range of 0.5-1.0, depending on the desired clustering granularity. Cluster-specific markers were identified using FindAllMarkers, retaining only positively enriched markers and applying a minimum effect-size threshold (avg_log2FC >2) to define robust cellular signatures. Cell populations were annotated based on the differential expression of canonical protein markers, such that cells with high expression of CD3 and CD8a were classified as CD8 T lymphocytes, $CD3^+$ $PD\text{-}1^+$ cells as PD-1-positive T cells, Pan-$cytokeratin^+$/E-$cadherin^+$ cells as epithelial/neoplastic cells, $PD\text{-}L1^+$ cells as PD-L1-positive tumor cells, $CD163^+$ cells as M2 macrophages, $aSMA^+$/Collagen I^+ cells as fibroblasts, Granzyme B^+ cells as cytotoxic/NK cells, $CD117^+$ (c-Kit) cells as c-Kit-positive cells, Cleaved caspase-3^+ cells as apoptotic cells, Pan-$cytokeratin^+$/$Ki67^+$ as tumor proliferative and $CD3^+$/$FOXP3^+$ as regulatory T cells (Treg).

Spatial features, including the number of neighboring cells and cell area, were aggregated at the cell-type level and compared across clinical conditions, including HPV status. Results were visualized using spatial marker maps, annotated UMAPs, and heatmaps integrating average marker expression, cluster identity, and clinical metadata.

Single-cell RNAseq validation

Publicly available single-cell RNA-seq data from 23 patients diagnosed with head and neck squamous cell carcinoma and annotated for HPV status (16 HPV-negative and 7 HPV-positive) were used for validation (GEO accession GSE181919 [28]) (**Figure 1**). Preprocessed count matrices provided by the original authors were imported into Seurat, and 54,239 previously annotated cells were retained for downstream analyses. No additional quality control filtering was applied.

Cell-cell communication was inferred using the CellChat R [29] package from the annotated Seurat object, with HPV-positive and HPV-negative samples analyzed separately. For each group, CellChat objects were constructed using CellChatDB. human database within the same package, and overexpressed ligands, receptors, and interactions were identified. Communication probabilities were estimated using the triMean method, adjusted for population size, and interactions involving cell types with fewer than 20 cells were excluded. Aggregated networks were compared to assess interaction strength, active signaling pathways, dominant sender and receiver cell types, and shared or group-specific pathways.

Trajectory inference was performed on T cells using the Monocle3 R package [30,31]. T cells were subsetted, reclustered, and marker genes were identified using Seurat's FindAllMarkers. Cluster 9, enriched for naïve T cell markers, was selected as the root state. Count matrices and metadata were converted into a cell data set object, followed by preprocessing, principal graph learning, and pseudotime ordering. Genes associated with trajectory progression were identified using graph-based tests and grouped into co-expression modules to characterize dynamic transcriptional programs in relation to HPV status.

Data availability

The manuscript and its additional information contain the data that support the study's conclusions. The NCBI Gene Expression Omnibus (GSE318768) contains 450K array DNA methylation raw data (IDAT files) and normalized Beta values matrix produced for this investigation.

Code availability

The code used to generate the results presented in this manuscript is available as a public repository (https://github.com/felipeluz97/IMC-data-analysis/tree/main).

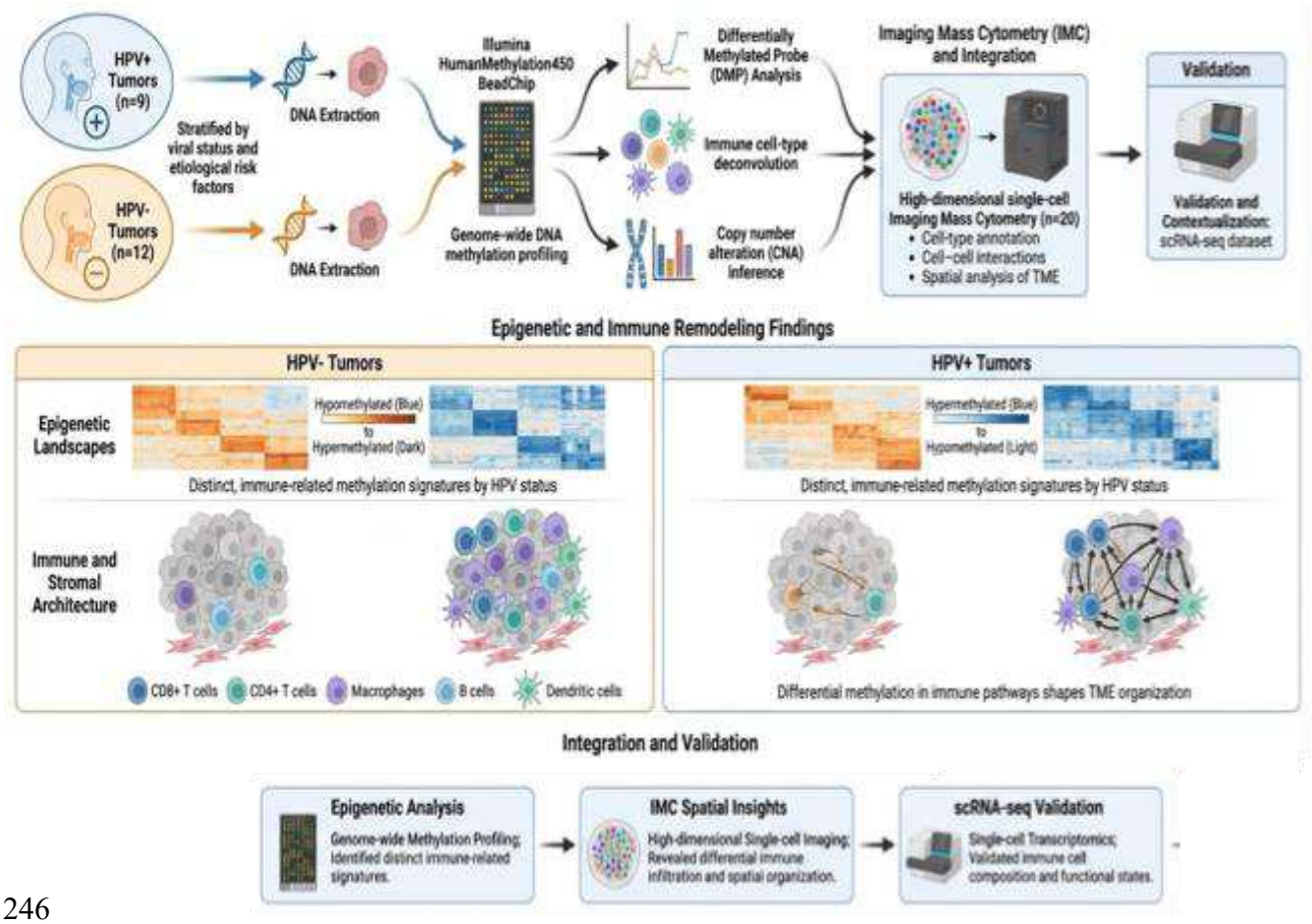


Figure 1. Patients were stratified according to established etiological risk factors and classified as HPV-positive (HPV+) or HPV-negative (HPV-). Genome-wide DNA methylation profiling using the Illumina HumanMethylation450 BeadChip was performed on 21 tumors (12 HPV-negative, 9 HPV-positive). Raw methylation data were leveraged for differential methylation probe (DMP) analysis, immune cell-type deconvolution, and inference of copy number alterations (CNAs). Imaging mass cytometry (IMC) was conducted on 20 HNC samples to spatially interrogate the tumor microenvironment (TME) and integrate epigenetic insights with single-cell–resolved tissue architecture. IMC data were used for cell-type annotation, inference of cell–cell interactions, identification of tumor and stromal communities, and spatial analysis of the TME. An independent single-cell RNA sequencing dataset was used to validate and further contextualize the findings.

Results

Differentially methylated probes (DMP) between HPV+ and HPV- tumors

HNC exhibits distinct epigenetic landscapes that reflect their underlying etiological drivers. Hierarchical clustering of the 10,000 CpG sites exhibiting the highest inter-sample variance (ranked by standard deviation) revealed a clear segregation of tumors according to HPV status (**Figure 2A**), indicating that viral infection is associated with distinct epigenetic landscapes. To further interrogate these differences, we identified differentially methylated positions (DMPs) between HPV-positive and HPV-negative tumors.

A total of 770 DMPs were detected ($p < 0.05$, $|logFC| > 0.2$), of which 528 were hypomethylated and 242 hypermethylated in HPV-positive tumors, corresponding to 386 annotated genes. Genomic distribution analysis revealed that 54 DMPs were located in first exons, 23 in 3′ untranslated regions (3′UTRs), 64 in 5′UTRs, 215 within gene bodies, 222 in intergenic regions, 98 within 1,500 base pairs upstream of transcription start sites (TSS), and 94 within 200 base pairs upstream of TSS. Notably, 397 DMPs overlapped CpG islands (**Supplemental Table 4**).

Pathway enrichment analysis was performed using the C7 immunologic signature collection from the Molecular Signatures Database (MSigDB), focusing on genes associated with hypomethylated DMPs in each group as putative overexpressed candidates. This revealed that HPV-positive tumors are enriched for hypomethylated genes linked to TLR4-mediated innate inflammatory signaling, TH2-skewed adaptive immune activation, and pro-inflammatory regulatory T cell (Treg) effector states. In contrast, HPV-negative tumors displayed enrichment for signatures indicative of delayed TLR1/2-mediated monocyte activation, classical humoral adaptive responses, and acute systemic immune activation following vaccination (**Figure 2B**).

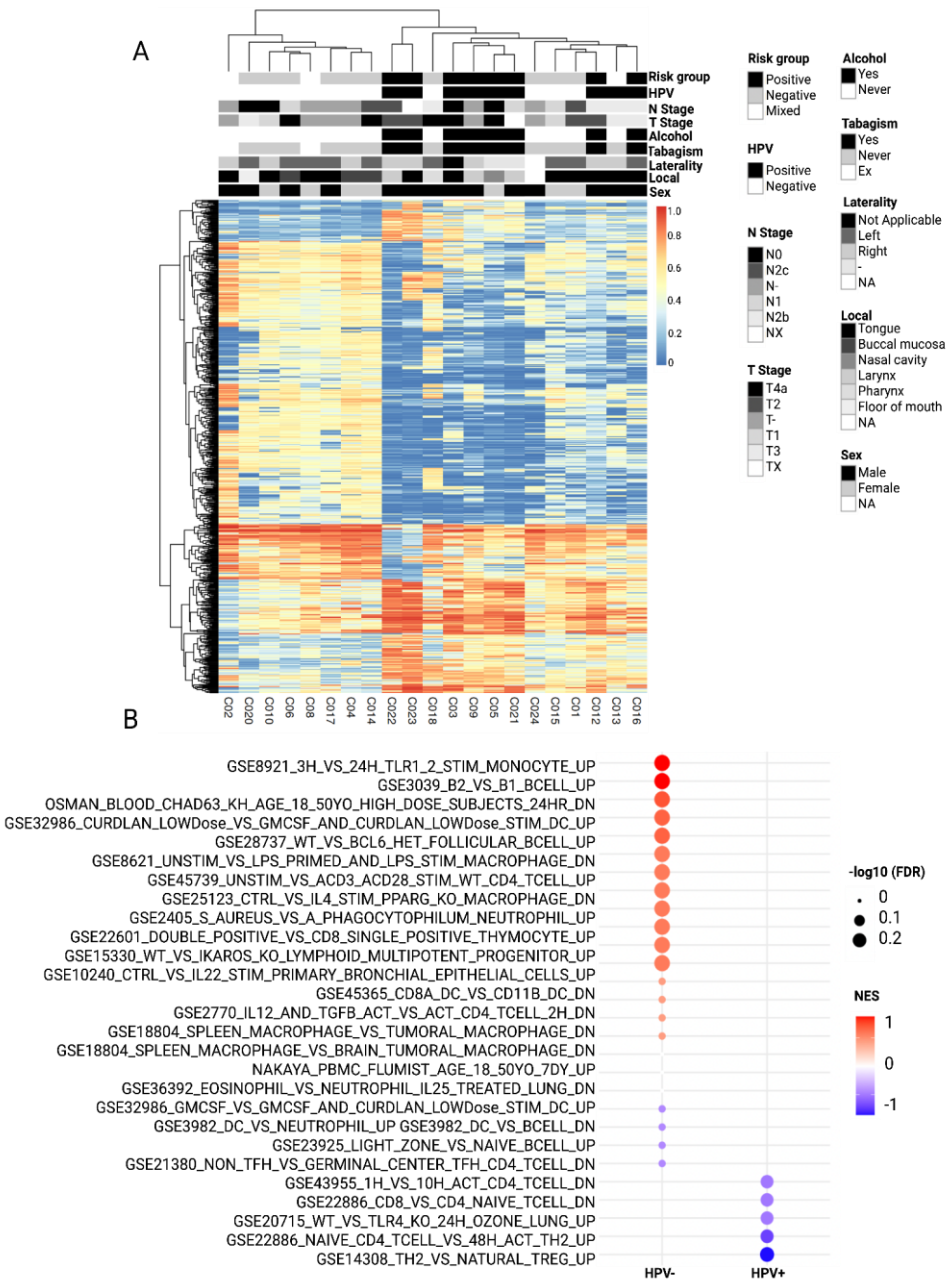


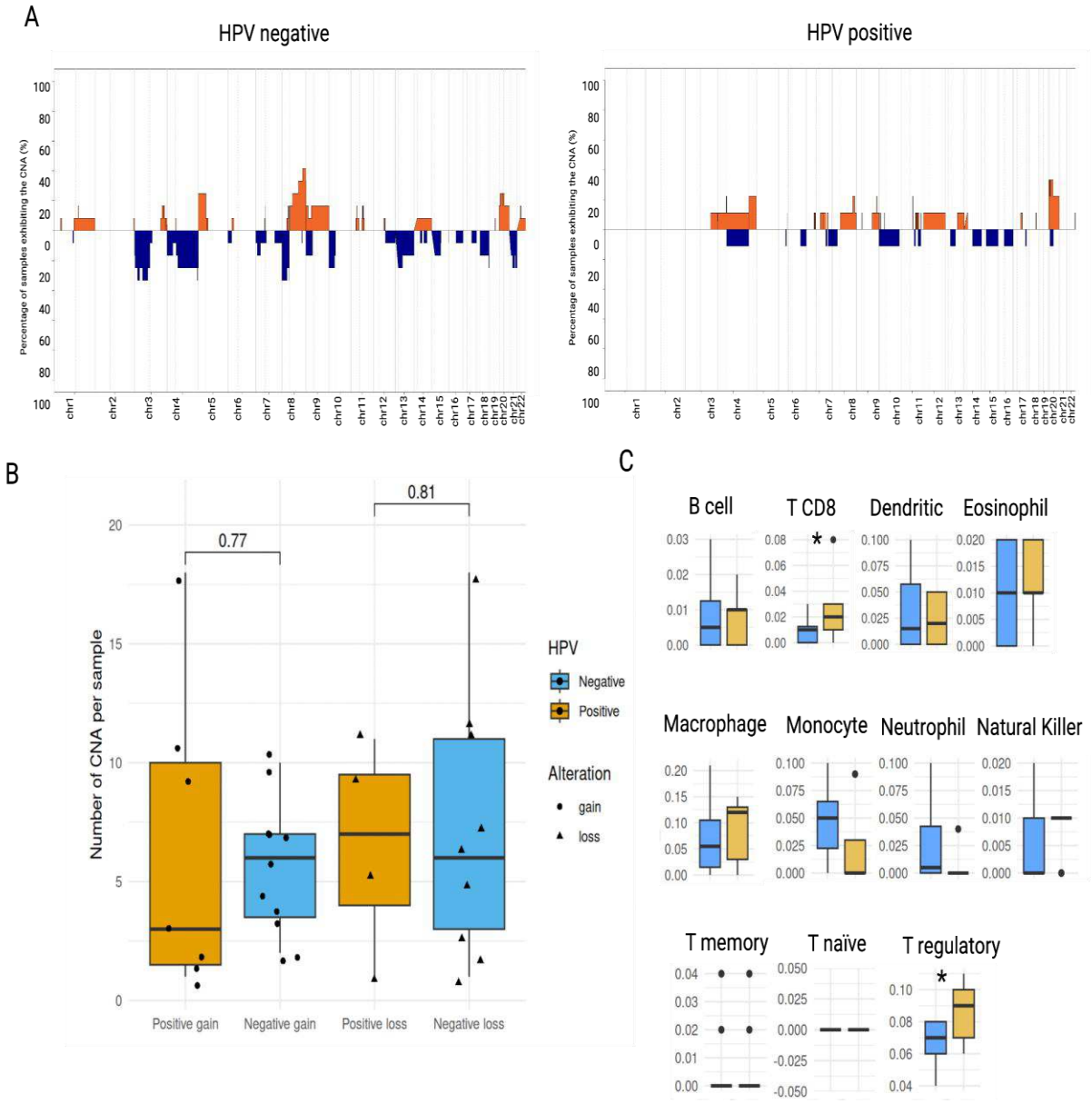
Figure 2. DNA methylation profiling of HPV+ *versus* HPV- tumors. A) Hierarchical clustering and heatmap of the 10,000 CpG sites with the highest inter-sample variance, ranked by standard deviation. Samples are annotated according to clinical characteristics. B) Pathway enrichment analysis based on hypomethylated differentially methylated positions (DMPs) from each group, annotated against the C7 immunologic signature gene set collection from the Molecular Signatures Database (MSigDB). T stage, Tumor stage (T1, T2: Early-stage; T3, T4:

Advanced-stage); N stage, Lymph Node stage (N1, N2: Early-stage; N2, N3: Advanced-stage). Created with BioRender.com (o99u352).

Copy number alterations (CNA) in relation to tumor infiltrating lymphocytes deconvolution

Copy number alterations (CNAs) were analyzed to assess whether the differences observed in inflammatory signatures could be linked to differential tumor immunogenicity driven by neoantigen formation due to the genomic instability. To this end, CNAs were extracted from the raw methylome data (IDAT files) and analyzed according to the HPV status. Although different CNA profiles were observed between the two groups with HPV-positive tumors exhibiting a slightly more unstable pattern with alterations distributed across the genome and higher percentage of samples altered, and HPV-negative tumors showing more localized alterations confined to specific chromosomes (**Figure 3A**), the overall number of copy number gains and losses did not differ significantly between groups (**Figure 3B**).

The beta-value matrix was submitted to immune cell deconvolution analysis that identified 11 immune cell types across all tumors. This analysis allowed inference of the absolute abundance of each cellular component and revealed that HPV-positive tumors harbor significantly higher levels of regulatory T cells (Tregs) and $CD8^+$ T cells compared with HPV-negative tumors (**Figure 3C**).



307

308 **Figure 3. Copy number alteration profile and inflammatory infiltrate.** A) Percentage of
309 CNAs detected in the genome across all samples. The x axis represents chromosomes, and
310 the y axis indicates the percentage of samples harboring each alteration. Tumors are stratified
311 as HPV-negative (left panel) and HPV-positive (right panel). B) Boxplot showing differences
312 in the total number of copy number alterations (gains and losses) between HPV-positive and
313 HPV-negative tumors. C) Boxplots illustrating differences in the absolute abundance of each
314 immune cell type between HPV-positive and HPV-negative tumors.Created with

BioRender.com (o99u352). T CD8 adjusted p-value: 0.048; T regulatory adjusted p-value: 0.036

Spatial distribution of tumor microenvironment components

To gain insight into the regulation of the tumor microenvironment in head and neck tumors, we profiled tumor-associated markers and canonical inflammatory cell markers in 20 tumors (12 HPV-positive and 8 HPV-negative) characterizing 209,302 individual cells. Cells were clustered based on the expression of cell-specific markers, batch effects were removed using the Seurat framework, and cell identities were assigned according to canonical markers. Overall, UMAP visualization revealed no clustering driven by batch effects, either by patient of origin or HPV infection status (**Figure 4A–F**).

Seventeen cell clusters were identified, corresponding to 10 annotated cell types (**Figure 4D).** To assess differences in tumor microenvironment composition between HPV-positive and HPV-negative tumors, we performed an initial analysis of the relative frequency of each cellular entity. This analysis revealed subtle differences in the abundance of PD-L1-expressing tumor cells and $CD8^+$ T lymphocytes in HPV-infected tumors (**Figure 4G**). These differences became more pronounced when absolute cell frequencies were compared (**Figure 4H**), revealing that HPV-positive tumors harbor a more prominent inflammatory infiltrate, enriched for $CD8^+$ T lymphocytes.

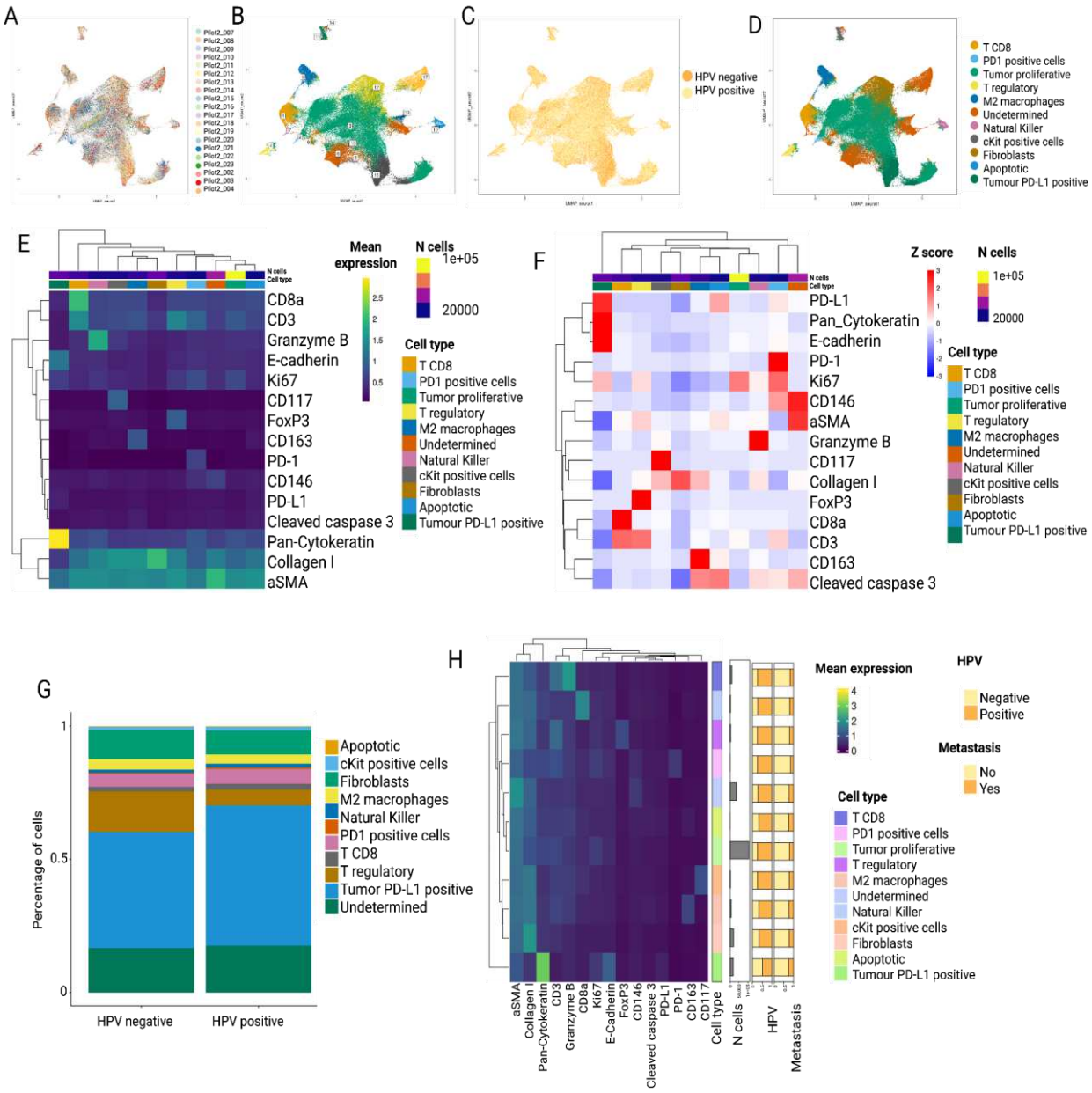


Figure 4. Immune mass cytometry analysis and cell type annotation. A-D) UMAP projections colored by patient of origin, cluster identity, HPV infection status, and cell type annotation, respectively. **E-F**) Hierarchical clustering and heatmaps of the identified clusters, with columns representing cell clusters and rows representing markers **e** shows the mean expression of each marker per cluster, and **f** displays Z-score-normalized expression values. **G**) Bar plot showing the relative frequency of each cell type in HPV-positive and HPV-negative tumors. **H**) Complex heatmap depicting hierarchical clustering of cell clusters based on the

mean expression of canonical markers. Clusters are annotated by cell number, HPV infection status, and presence of metastasis. Created with BioRender.com (o99u352).

Once we identified differences in the cellular composition of the tumor microenvironment between HPV-positive and HPV-negative tumors, we investigated how these cells are spatially distributed within the tumor tissue. Following annotation, cells were plotted in two-dimensional space using pixel coordinates obtained from the Imaging Mass Cytometer System (IMC™, Fluidigm, USA). Overall, HPV-negative tumors displayed a more immunologically "cold" phenotype, characterized by reduced inflammatory infiltrates but enriched in fibroblasts, as evidenced by high collagen I expression. These fibroblasts frequently surrounded tumor cells, identified by pan-cytokeratin expression (red), and appeared to restrict the access of inflammatory cells to the tumor niche (**Figure 5A**). In contrast, HPV-positive tumors exhibited more proliferative tumor niches, as indicated by elevated Ki67 expression, together with a high density of infiltrating lymphocytes, marked in blue by CD3 expression, which appeared to recognize tumor cells and more readily infiltrate the tumor core (**Figure 6A**).

IMC data further enabled the inference of cellular communities and their spatial organization. HPV-negative tumors exhibited a more homogeneous microenvironment, both in tumor-associated and stromal cellular communities (**Figure 5B-C**). Conversely, HPV-positive tumors displayed increased spatial heterogeneity, with multiple distinct tumor and stromal communities coexisting within the same tissue sections (**Figure 6B-C**).

Regarding cell-cell interactions, HPV-negative tumors showed predominant direct crosstalk between tumor cells and fibroblasts, effectively isolating lymphocytes that appeared unable to penetrate the tumor core (**Figure 5D**). In HPV-positive tumors, increased interactions between tumor cells and lymphocytes, particularly $CD8^+$ T cells, were observed. Although fibroblasts were present, they appeared more dispersed throughout the tumor microenvironment (**Figure 6D**).

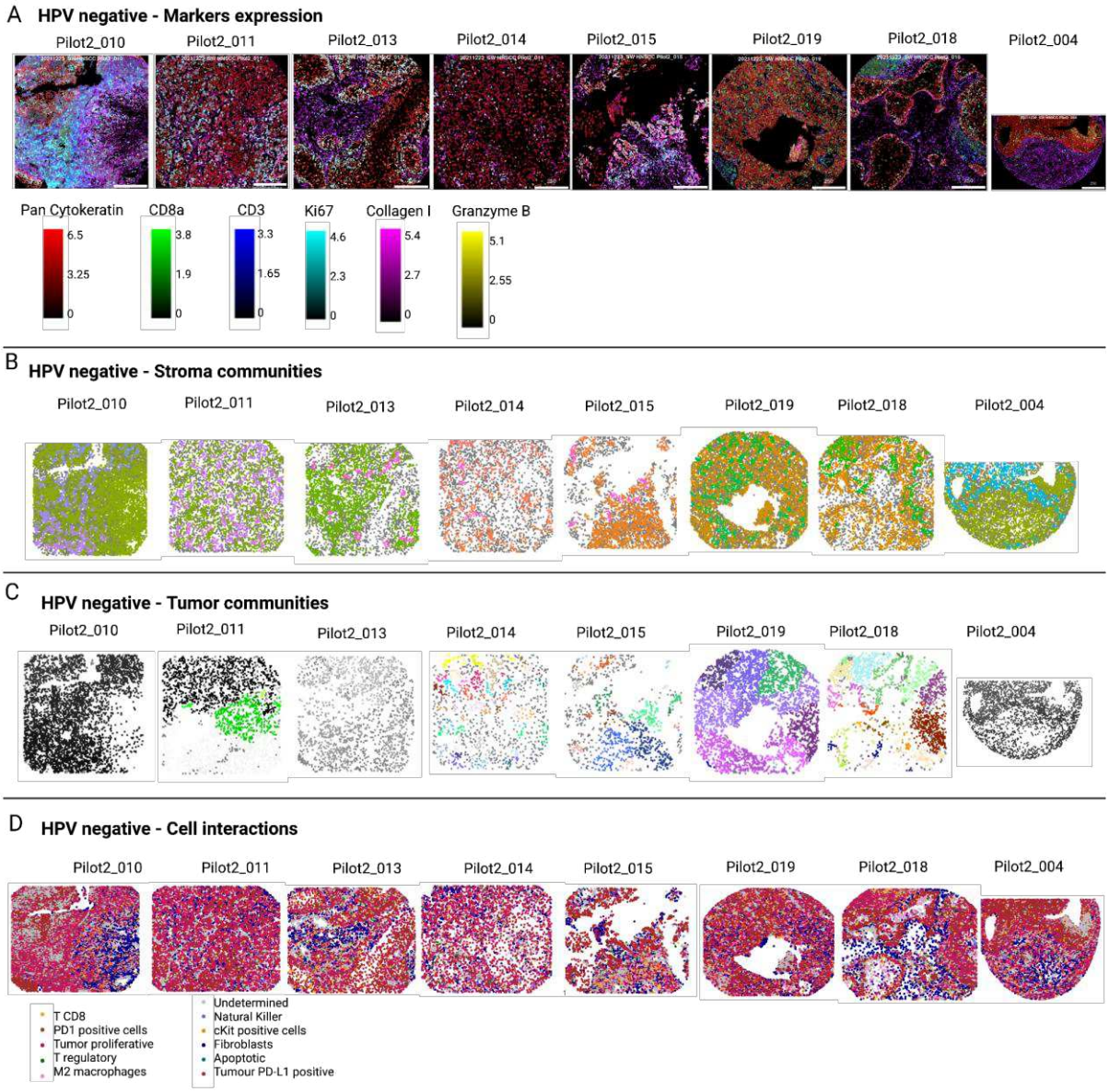


Figure 5. Spatial organization of the HPV-negative tumor microenvironment. A) Expression of key markers used for cell annotation visualized in a two-dimensional spatial context that recapitulates the histological tissue section. B-C) Identified stromal cellular communities. Each community is represented by a distinct color; increased color diversity reflects higher spatial heterogeneity of the tumor microenvironment. D) Cell-cell interaction network. Each color denotes a distinct cell type, and putative interactions are represented by gray lines connecting individual cells. Created with BioRender.com (o99u352).

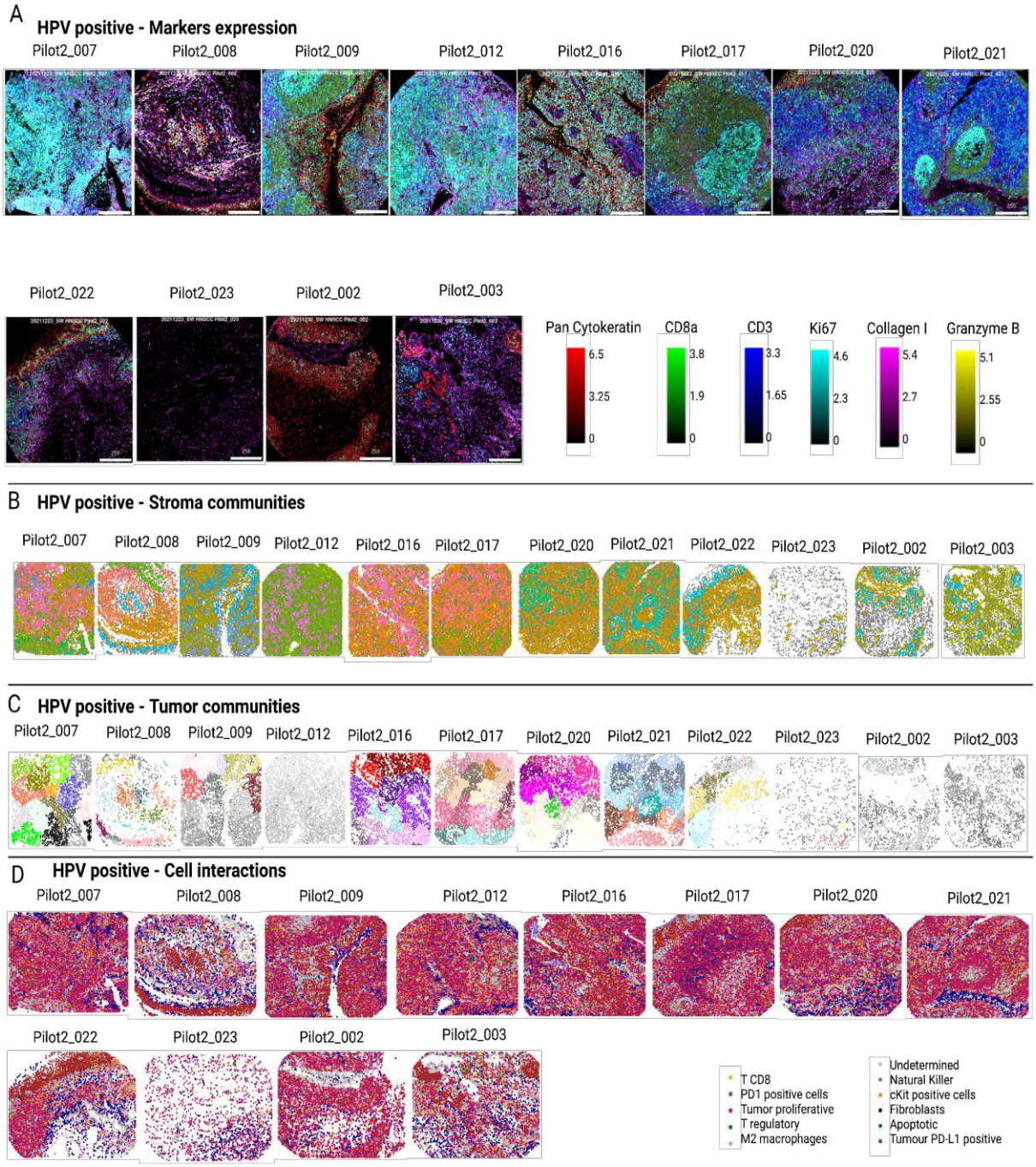


Figure 6. Spatial organization of the HPV-positive tumor microenvironment. A) Expression of key markers used for cell annotation visualized in a two-dimensional spatial context that recapitulates the histological tissue section. B-C) Identification of stromal cellular communities. Each community is represented by a distinct color; increased color diversity reflects higher spatial heterogeneity of the tumor microenvironment. D) Cell-cell interaction

network. Each color denotes a distinct cell type, and putative interactions are represented by gray lines connecting individual cells. Created with BioRender.com (o99u352).

Independent cohort validation of cell-interaction and cell trajectory analysis

To validate our findings regarding the tumor microenvironment in our cohort, derived from both methylome and IMC analyses, we analyzed an independent cohort of head and neck tumors in which tumor microenvironment cells had been previously characterized, clustered, and annotated using single-cell RNA sequencing (scRNA-seq) data (GEO accession GSE181919). Original cell annotations were retained, and additional cell-cell communication and trajectory analyses were performed.

From 54,239 cells, 32,292 originated from HPV-negative tumors and 21,947 from HPV-positive tumors. The primary aim of this analysis was to further elucidate mechanisms that facilitate tumor cell recognition by inflammatory components, particularly T lymphocytes, in HPV-positive tumors. Within this dataset, 17,869 T lymphocytes were identified, 8,580 from HPV-negative tumors and 9,289 from HPV-positive tumors, and were used for subsequent analyses **(Figure 7A**).

Cell-cell communication analysis revealed that HPV-negative tumors presented the strongest interactions between fibroblasts and T lymphocytes, consistent with our previous observations. A prominent interaction between fibroblasts and malignant cells was also detected. In contrast, while HPV-positive tumors also displayed strong fibroblast-T lymphocyte interactions, autocrine signaling among T lymphocytes was markedly increased, suggesting enhanced T cell self-regulation. Although more subtle, an increase in interactions between T lymphocytes and malignant cells was also observed, indicating improved tumor cell recognition in this context. Concurrently, interactions between fibroblasts and malignant cells were modestly reduced (**Figure 7B-C**).

When comparing the number of signals sent and received by each cell type, a similar overall pattern emerged in both tumor groups: T lymphocytes were the predominant signal

receivers, whereas fibroblasts were the primary signal senders, however, showing a notable signal intensity difference between HPV-negative and HPV-positive tumors. In HPV-positive tumors, T lymphocytes exhibited a twofold increase in both received and emitted signaling intensity compared with HPV-negative tumors, further supporting the notion of enhanced T cell autocrine regulation. Other inflammatory cell types displayed comparable signaling intensities across both tumor groups. In contrast, neoplastic cells showed a proportional increase in received signaling intensity, surpassing that of inflammatory cells, suggesting heightened immune recognition in HPV-positive tumors (**Figure 7D**).

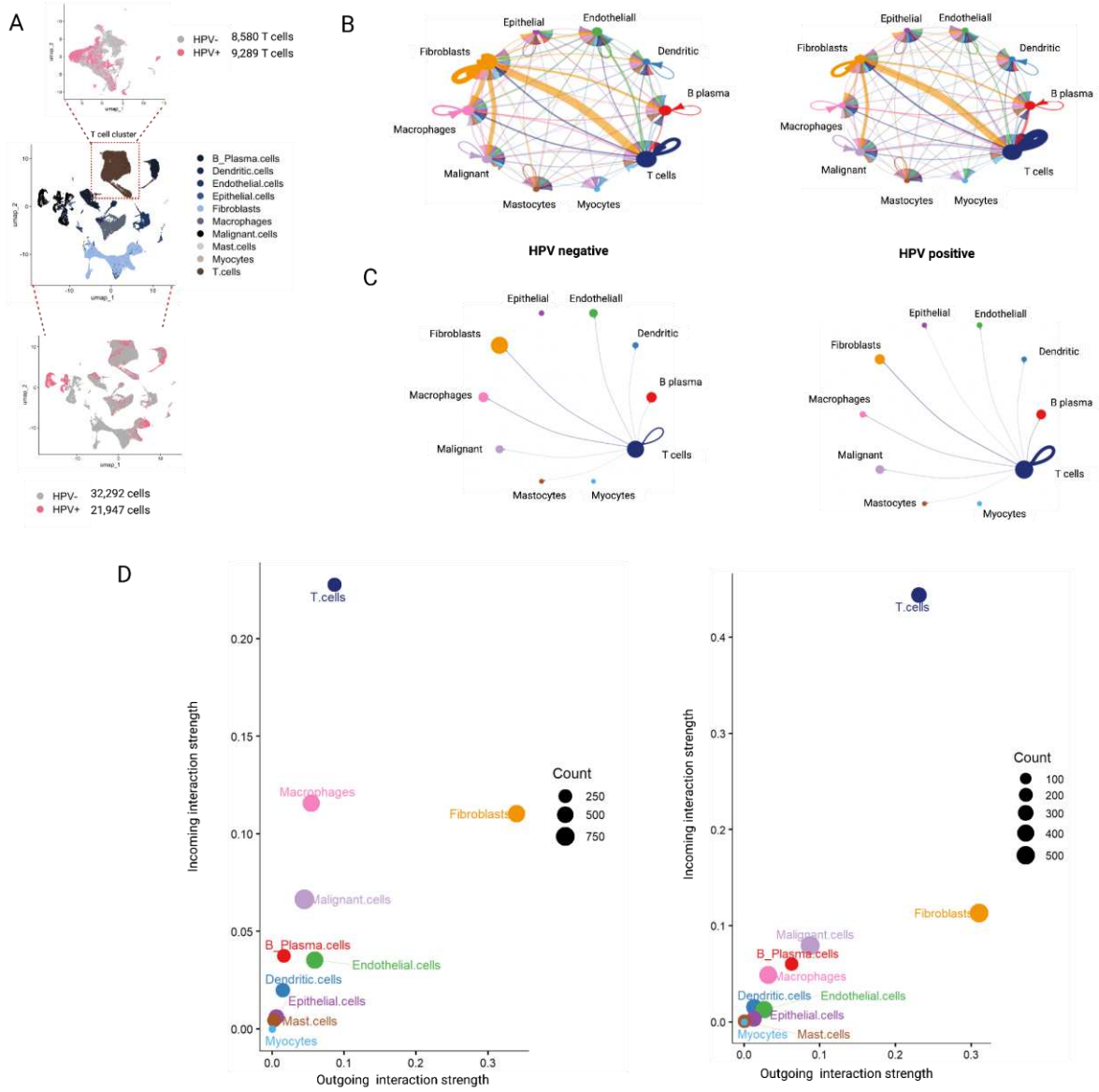


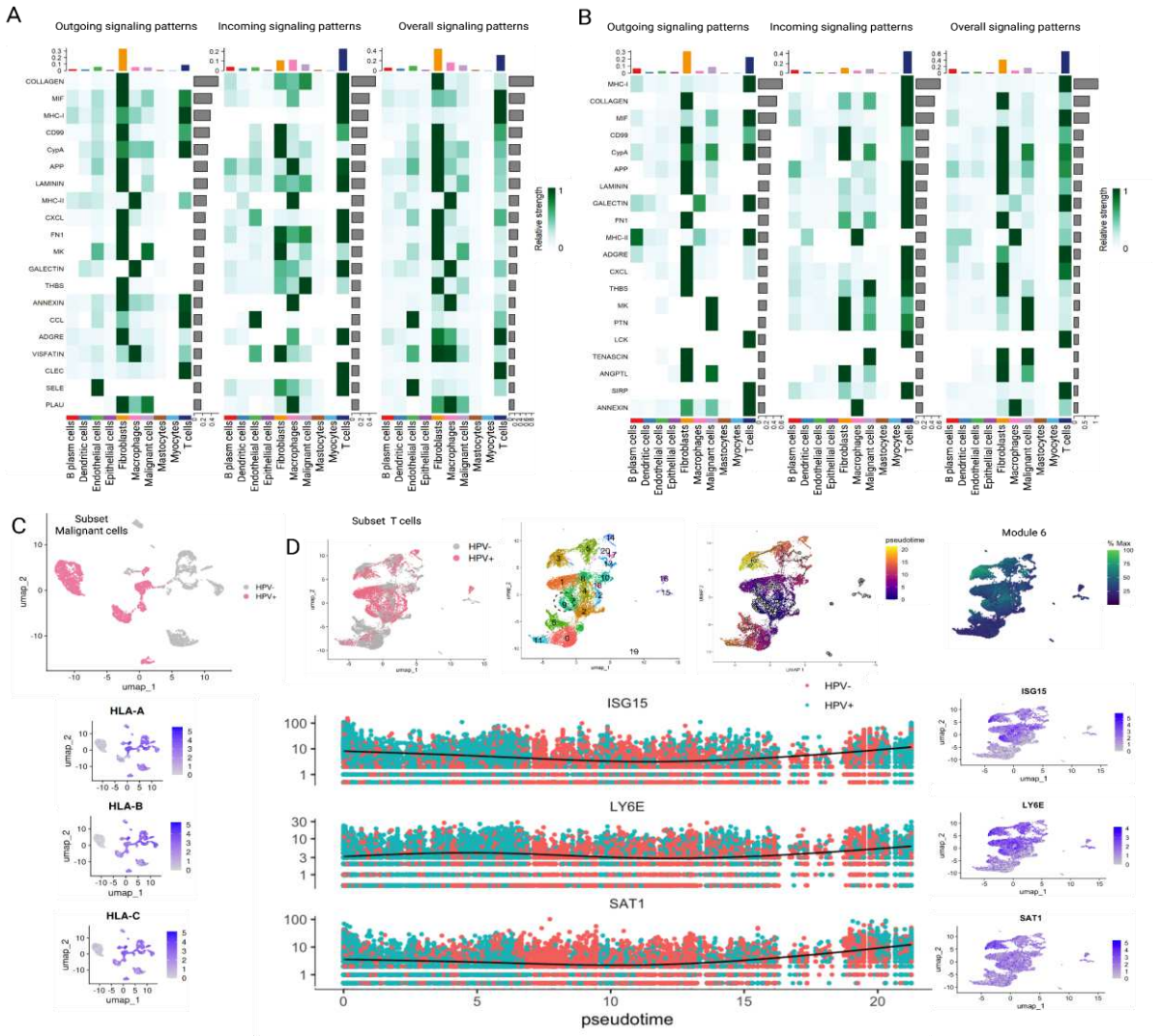
Figure 7. Cell-cell interaction analysis in an independent scRNA-seq cohort. A) UMAP showing the identified cell clusters in the dataset, highlighting the total number of cells derived from HPV-positive and HPV-negative tumors, as well as the number of T lymphocytes in each group. B) Cell-cell interaction network, in which nodes represent cell types and edges indicate total interaction strength (weights). C) Cell-cell interaction network focusing on T lymphocytes, with T cell-associated edges isolated to enable detailed visualization of total interaction strength (weights). D) Scatter plot showing HPV-negative and HPV-positive tumors, respectively, depicting signaling strength, with received signals on the y axis and emitted signals on the x axis. Created with BioRender.com (o99u352).

Cell-cell interaction analysis, leveraging a curated database comprising more than 3,000 ligand-receptor pairs, enables the identification of molecular mechanisms that promote intercellular communication [29]. Interrogation of these pathways revealed that, in HPV-negative tumors, the signals contributing most strongly to cellular interactions are associated with collagen-related pathways. These ligands are expressed by fibroblasts and preferentially received by T lymphocytes and neoplastic cells (**Figure 8A**).

In contrast, in HPV-positive tumors, the strongest interaction signals correspond to MHC class I ligands. However, these ligands appear to be primarily expressed by T lymphocytes and recognized in an autocrine manner, whereas signaling involving neoplastic cells is nearly undetectable (**Figure 8B**). Although the MHC class I pathway is weakly expressed in HPV-negative tumors, it remains detectable in HPV-negative neoplastic cells, suggesting that these cells retain the potential to be recognized by the immune system; nonetheless, the presence of a fibroblast-rich barrier may contribute to immune evasion in this context. Consistent with this model, we demonstrate that neoplastic cells from HPV-positive tumors indeed show reduced expression of key MHC class I pathway components, including *HLA-A*, *HLA-B*, and *HLA-C* (**Figure 8C**).

To further elucidate mechanisms regulating T lymphocyte behavior in head and neck cancer, we performed a cellular trajectory analysis. T lymphocytes were subsetted from the dataset, yielding 20 clusters, which were subjected to differential expression analysis. Cluster 9 was selected as the root of the trajectory due to its enrichment for naïve T cell markers, including *CCR7* (**Figure 8D, Supplemental Table 5**). Using pseudotime analysis, we sought to identify gene programs associated with the evolutionary trajectory of these T lymphocytes. We identified nine gene modules (**Supplemental Table 6**); among them, module 6 was particularly notable, as it exhibited mean expression dynamics concordant with pseudotime progression and comprised genes characteristic of canonical type I and type II interferon response signatures in T cells, such as *ISG15*, *LY6E*, and *SAT1*. This signature was less pronounced in T lymphocytes from HPV-negative tumors and markedly enriched in those from HPV-positive tumors (**Figure 8D**).

To better understand the role of fibroblasts in the tumor context, we subset these cells and performed differential gene expression analysis between fibroblasts from HPV-positive and HPV-negative tumors identifying 318 differentially expressed genes (out of 8,755, adjusted p-value <0.05 and log2FC >3). We highlight that fibroblasts from HPV-positive tumors showed higher expression of *KRT14, PTK7, GREM1* and *SFRP1*, whereas fibroblasts from HPV-negative tumors exhibited higher expression of *PCOLCE2, C1QTNF3, THBD, WNT10B, FABP3* and *ALDH1A3* (**Supplemental Figure 1** and **Supplemental Table 7**).



463

464 **Figure 8. Cell-cell communication and trajectory analysis.** A-B) Heatmaps showing the
465 major ligand-receptor pairs involved in cell-cell communication. Columns represent cell types
466 and rows represent signaling pathways, with color intensity indicating signal strength. Panels
467 display emitted signals, received signals, and combined interactions, shown separately for
468 HPV-negative and HPV-positive tumors, respectively. C) Top panel shows a UMAP of a
469 subset of malignant cells colored by HPV infection status, highlighting the three main genes
470 involved in the MHC class I pathway, demonstrating reduced expression in HPV-positive
471 cancer cells. D) Cellular trajectory analysis of T lymphocytes. The top panels display UMAPs
472 of T cells colored by HPV infection status, root cluster identification, pseudotime, and gene
473 module 6, respectively. The bottom panels show cells ordered along pseudotime on the x axis,
474 colored by HPV infection status, highlighting the expression of the three hallmark genes of

module 6 on the y axis with their corresponding cellular expression levels. Created with BioRender.com (o99u352).

Discussion

This study provides a high-dimensional spatial map of the tumor microenvironment in head and neck cancer using a multi-omic approach. By integrating epigenomic and spatial single-cell analyses, we comprehensively characterized cellular composition, interactions, and spatial neighborhoods, and correlated these features with HPV infection status. Among the main risk factors associated with the onset and progression of HNC are tobacco use, alcohol consumption, and infection with human papillomavirus (HPV) [3,33]. The biological mechanisms underlying HNC development are highly complex, and alterations in DNA methylation profiles have been consistently associated with HNC pathogenesis ([9,34,35]. In this study, we leveraged genome-wide DNA methylation data generated using the Illumina HumanMethylation450K array to identify HPV-associated epigenetic alterations in HNC. These changes suggested a potential link between HPV-driven epigenetic regulation and modulation of the tumor microenvironment. To further investigate this relationship, we performed a detailed molecular and spatial characterization of the TME, integrating imaging mass cytometry and single-cell transcriptomic analyses.

Differentially methylated site analysis between HPV-positive and HPV-negative tumors revealed distinct epigenetic programs. HPV-negative tumors showed hypomethylation of genes associated with acute systemic immune activation following vaccination, classical humoral adaptive immunity, and delayed TLR1/2-mediated monocyte activation. In contrast, HPV-positive tumors exhibited hypomethylation of genes linked to TH2-type adaptive immune activation, TLR4-dependent innate inflammatory responses, and a pro-inflammatory effector state driven by regulatory T cells.

The pattern of hypomethylated genes observed in HPV-positive tumors suggests a more polarized, virus-driven immune response, in which persistent signals of chronic infection

preferentially activate specific inflammatory pathways while simultaneously promoting regulatory mechanisms. TH2 activation is typically associated with less cytotoxic immune responses [36], whereas the expansion or functional reprogramming of regulatory T cells (Tregs) can contribute to local immunosuppression even within an inflammatory microenvironment [37]. The hypomethylation of these pathways indicates that HPV infection not only activates immune responses but epigenetically reprograms them toward a state of controlled inflammation, potentially favoring viral persistence and tumor progression. Consistent with this model, HPV viral oncoproteins E6 and E7 have been shown to interact with epigenetic regulators, altering DNA methylation and chromatin organization at immune regulatory loci [38–40]. Integrative methylation profiling and immune deconvolution analyses revealed increased absolute frequencies of Tregs and $CD8^+$ T cells in HPV-positive tumors. Although tumors with high chromosomal instability are often more immunogenic due to increased neoantigen burden [41,42], we observed no significant differences in overall copy number alteration (CNA) burden between HPV-positive and HPV-negative tumors, indicating that modulation of the tumor microenvironment is unlikely to be driven by neoantigen-mediated immunogenicity.

To investigate the functional consequences of the methylation profiles, we examined the tumor microenvironment (TME) from a spatial perspective using imaging mass cytometry (IMC). HPV-positive tumors exhibited a more inflamed intratumoral microenvironment, with increased infiltration of immune cells, particularly $CD8^+$ T lymphocytes. Consistent with previous reports, HPV-positive tumors display an immunologically “hot” phenotype compared with HPV-negative “cold” tumors, characterized by enhanced T cell infiltration and immune regulatory features, which have been associated with improved clinical outcomes in HPV-associated head and neck cancer [43]. Spatially, HPV-positive tumors showed increased tumor cell proliferation and deeper penetration of T lymphocytes into the tumor core, whereas HPV-negative tumors were characterized by fibroblast-rich stromal barriers surrounding tumor nests, effectively limiting immune cell access to the tumor compartment.

Cell-cell interaction analysis revealed that in HPV-negative tumors, T cells engage predominantly with fibroblasts, whereas in HPV-positive tumors, T cells preferentially recognize tumor cells and exhibit autocrine regulatory interactions. Mechanistically, HPV-positive tumor cells display reduced MHC class I expression, while infiltrating T cells show canonical type I and II interferon responses. Overall, these data indicate that MHC class I downregulation in HPV-positive tumors limits antigen-specific $CD8^+$ T cell recognition. Consequently, although T cells are present within the tumor microenvironment and express interferon-associated signatures, their activation is largely bystander and cytokine-mediated rather than TCR–MHC I-dependent, resulting in a non-cytotoxic inflammatory state [44]. Single-cell RNA sequencing and spatial transcriptomics further reveal that HPV-positive tumors are enriched for fibroblasts with a fibroblastic reticular cell (FRC)-like phenotype, which localize to tertiary lymphoid structures [45].

Our data show that in HPV-negative tumors, fibroblasts surround the tumor niche and express genes linked to pro-tumoral stromal remodeling, negative regulation of differentiation pathways, and a chronically activated TME [46–48]. In contrast, fibroblasts in HPV-positive tumors display a more regulatory profile, associated with extracellular matrix organization, WNT signaling, and tissue homeostasis [49–53].

Conclusion

We proposed a model where HPV infection drives distinct epigenetic programs that shape the immune cell landscape of head and neck tumors in space and time-dependent manner (**Figure 9**). HPV-positive tumors showed hypomethylation of genes associated with TLR4-dependent innate inflammation, TH2-type adaptive responses, and Treg-mediated effector programs, whereas HPV-negative tumors were enriched for delayed TLR1/2 signaling, humoral immunity, and vaccine-like systemic immune activation signatures. These epigenetic differences correlate with downstream phenotypes, including increased immune infiltration,

enhanced T cell communication, interferon-driven T cell trajectories, and greater spatial between immune and cancer cells in HPV-positive tumors. In contrast, HPV-negative tumors exhibit fibroblast-driven collagen signaling, immune exclusion, and spatial compartmentalization that limit effective tumor recognition. Together, these findings indicate that HPV-associated epigenetic regulation coordinates immune activation and evasion through convergent molecular, cellular, and spatial mechanisms, which can be used for immune-based therapeutic strategies.

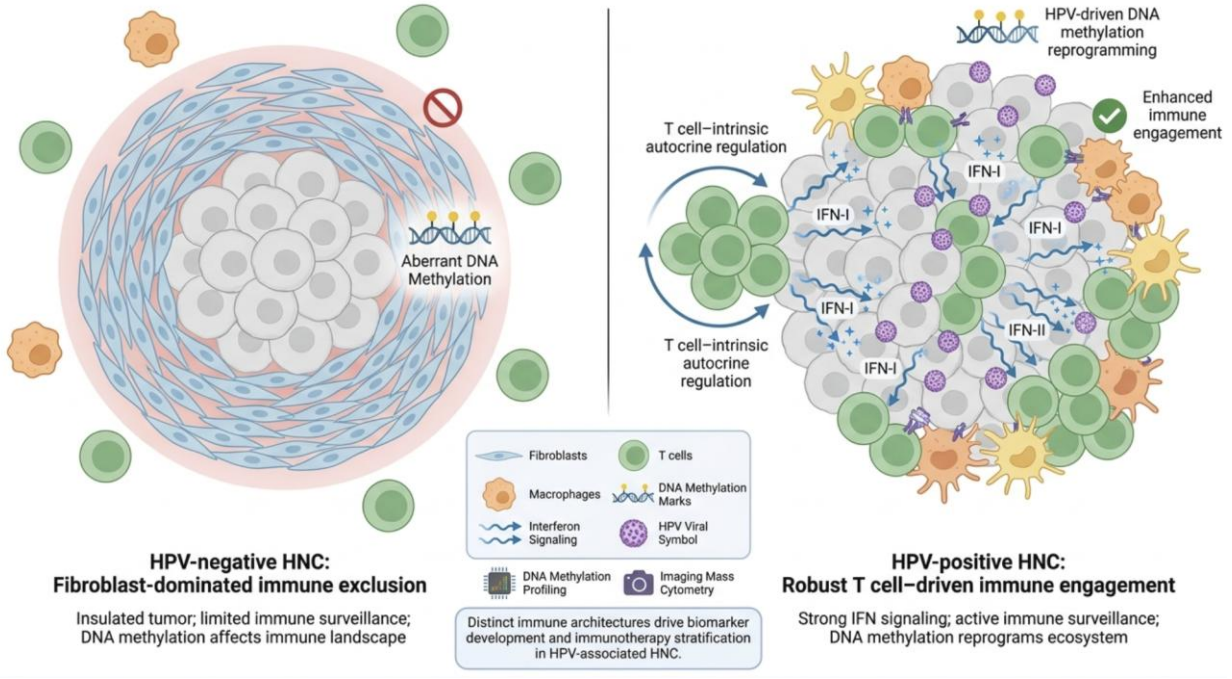


Figure 9. Proposed model of immune evasion by epigenetic modulation in head and neck tumors. **A**. A shielding mechanism. HPV-negative tumors are organized in nests where tumor cells are protected by a fibrotic stroma that hides tumor cells. **B**. A recognition mechanism where HPV reprograms the tumor cells epigenome to a pro-inflammatory and spatially accessible state.

Disclosure Statement

No disclosures were reported by any of the authors.

Authors' Contributions

F.L.T. Silva: Formal analysis, investigation, methodology, writing–review and editing. F. Farshadi: Data curation, visualization, writing–review and editing. M. Mascarella: Visualization, methodology, and editing. M. Alaoui-Jamali: Writing–review and editing. M. Hier: Resources, data curation, methodology, writing–review and editing. A. Mlynarek: Resources, data curation, methodology, writing–review and editing. M. Maschietto: Conceptualization, resources, data curation, software, formal analysis, supervision, validation, investigation, methodology, project administration, writing–review and editing. S.D. Silva: Conceptualization, resources, data curation, formal analysis, supervision, funding acquisition, validation, investigation, visualization, methodology, writing–original draft, project administration, writing–review and editing.

Fund information

This work was supported by CIHR-Project Grant (2022-2027) and RSBO/FRQ-S, NCOHR (New Frontier Seed Grant), DFATD - CBIE-FMPB. This research was made possible thanks to the support of the Dr. Arthur Rosenberg Memorial Fellowship Graduate Scholarship Fund (FF) and FAPESP (2022/04781-6 to FLTS and 2015/06281-7 to MM). The authors acknowledge all the valuable support from the Head and Neck Foundation (Jewish General Hospital, Faculty of Medicine, McGill University) and the Marvin Carsley Research Fund.

Acknowledgements

This study received technical support from core facilities from the Lady Davis Institute – Segal Cancer Center (Jewish General Hospital) and Rosalind and Morris Goodman Cancer Institute

(GCI) at McGill University, including the Research Pathology Core Facility (Dr Naciba Benlimame) and the Single Cell and Imaging Mass Cytometry Platform (SCIMAP -Yuhong Wei). The authors would like to acknowledge all the patients who participated in this study.

References

1. Barsouk, A., Aluru, J. S., Rawla, P., Saginala, K. & Barsouk, A. Epidemiology, risk factors, and prevention of head and neck squamous cell carcinoma. *Med. Sci. (Basel)* **11**, 42 (2023).
2. Pytynia, K. B., Dahlstrom, K. R. & Sturgis, E. M. Epidemiology of HPV-associated oropharyngeal cancer. *Oral Oncol.* **50**, 380–386 (2014).
3. Kowalski, L. P. *et al.* Head and neck cancer: Emerging concepts in biomarker discovery and opportunities for clinical translation. *Clin. Transl. Med.* **10**, e209 (2020).
4. Sharon, S., Daher-Ghanem, N., Zaid, D., Gough, M. J. & Kravchenko-Balasha, N. The immunogenic radiation and new players in immunotherapy and targeted therapy for head and neck cancer. *Front. Oral Health* **4**, 1180869 (2023).
5. Johnson, D. E. *et al.* Head and neck squamous cell carcinoma. *Nat. Rev. Dis. Primers* **6**, 92 (2020).
6. Ghiani, L. & Chiocca, S. High risk-Human Papillomavirus in HNSCC: Present and future challenges for epigenetic therapies. *Int. J. Mol. Sci.* **23**, 3483 (2022).
7. Lechner, M., Liu, J., Masterson, L. & Fenton, T. R. HPV-associated oropharyngeal cancer: epidemiology, molecular biology and clinical management. *Nat. Rev. Clin. Oncol.* **19**, 306–327 (2022).
8. Xiao, C. *et al.* Association of epigenetic age acceleration with risk factors, survival, and quality of life in patients with head and neck cancer. *Int. J. Radiat. Oncol. Biol. Phys.* **111**, 157–167 (2021).

9. Hier, J. *et al.* Portrait of DNA methylated genes predictive of poor prognosis in head and neck cancer and the implication for targeted therapy. *Sci. Rep.* **11**, 10012 (2021).
10. Morand, G. B. *et al.* Molecular prognostic indicators in HPV-positive oropharyngeal cancer: an updated review. *Clin. Exp. Metastasis* **39**, 407–416 (2022).
11. McMahon, K. W., Karunasena, E. & Ahuja, N. The roles of DNA methylation in the stages of cancer. *Cancer J.* **23**, 257–261 (2017).
12. Lakshminarasimhan, R. & Liang, G. The role of DNA methylation in cancer. *Adv. Exp. Med. Biol.* **945**, 151–172 (2016).
13. Yang, J. *et al.* Epigenetic regulation in the tumor microenvironment: molecular mechanisms and therapeutic targets. *Signal Transduct. Target. Ther.* **8**, 210 (2023).
14. Liang, Y. & Turcan, S. Epigenetic drugs and their immune modulating potential in cancers. *Biomedicines* **10**, 211 (2022).
15. Qin, Y., Zheng, X., Gao, W., Wang, B. & Wu, Y. Tumor microenvironment and immune-related therapies of head and neck squamous cell carcinoma. *Mol. Ther. Oncolytics* **20**, 342–351 (2021).
16. Zhao, H. *et al.* Inflammation and tumor progression: signaling pathways and targeted intervention. *Signal Transduct. Target. Ther.* **6**, 263 (2021).
17. Neophytou, C. M., Panagi, M., Stylianopoulos, T. & Papageorgis, P. The role of tumor microenvironment in cancer metastasis: Molecular mechanisms and therapeutic opportunities. *Cancers (Basel)* **13**, 2053 (2021).
18. Baghban, R. *et al.* Tumor microenvironment complexity and therapeutic implications at a glance. *Cell Commun. Signal.* **18**, 59 (2020).
19. Fares, J., Fares, M. Y., Khachfe, H. H., Salhab, H. A. & Fares, Y. Molecular principles of metastasis: a hallmark of cancer revisited. *Signal Transduct. Target. Ther.* **5**, 28 (2020).
20. Daenekas, B. *et al.* Conumee 2.0: enhanced copy-number variation analysis from DNA methylation arrays for humans and mice. *Bioinformatics* **40**, (2024).
21. Aryee, M. J. *et al.* Minfi: a flexible and comprehensive Bioconductor package for the analysis of Infinium DNA methylation microarrays. *Bioinformatics* **30**, 1363–1369 (2014).

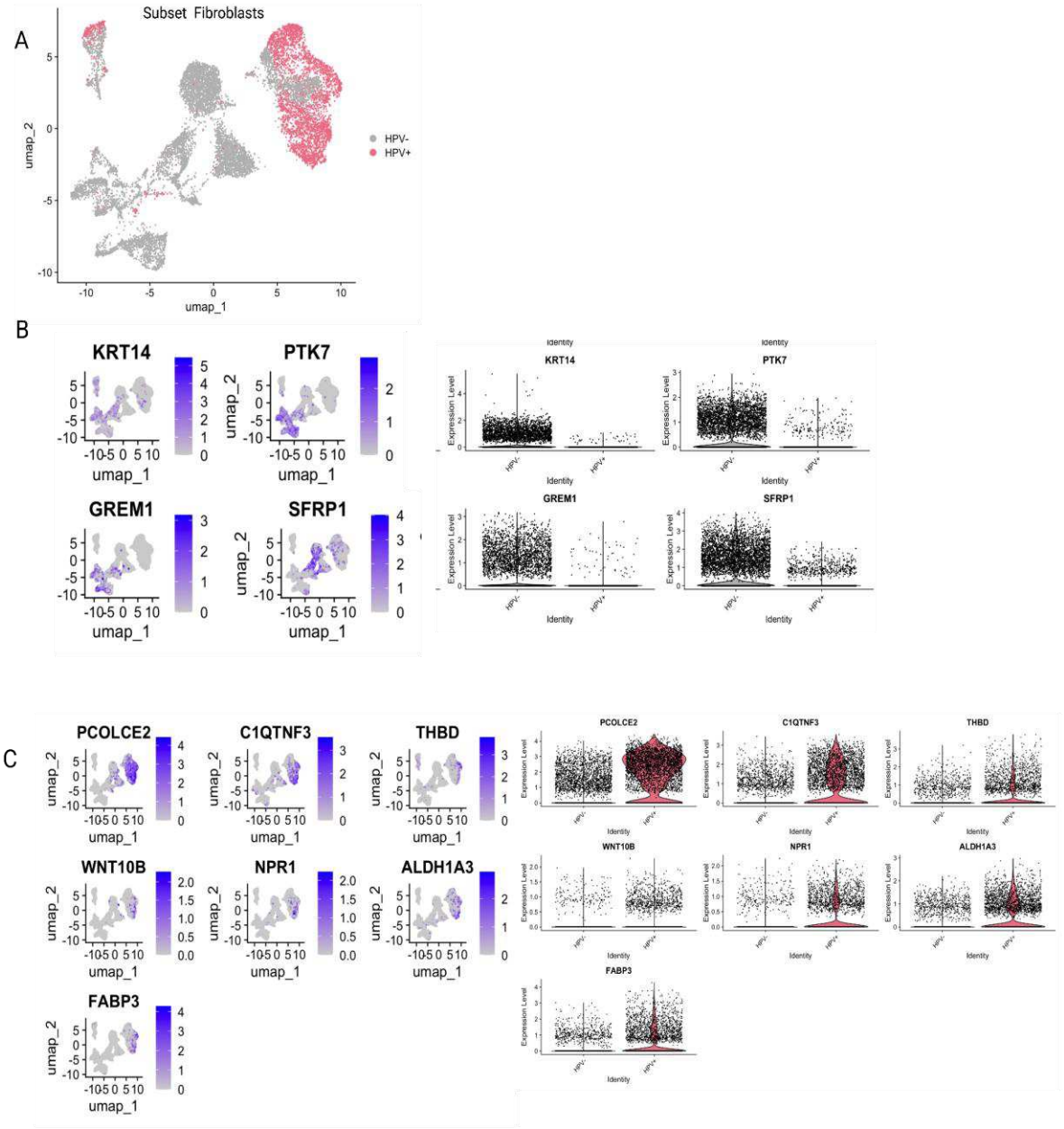
22. Fortin, J.-P. *et al.* Functional normalization of 450k methylation array data improves replication in large cancer studies. *bioRxiv* (2014) doi:10.1101/002956.
23. Arneson, D., Yang, X. & Wang, K. MethylResolver-a method for deconvoluting bulk DNA methylation profiles into known and unknown cell contents. *Commun. Biol.* **3**, 422 (2020).
24. Karimi, E. *et al.* Single-cell spatial immune landscapes of primary and metastatic brain tumours. *Nature* **614**, 555–563 (2023).
25. Windhager, J. *et al.* An end-to-end workflow for multiplexed image processing and analysis. *Nat. Protoc.* **18**, 3565–3613 (2023).
26. Kuett, L. *et al.* Three-dimensional imaging mass cytometry for highly multiplexed molecular and cellular mapping of tissues and the tumor microenvironment. *Nat. Cancer* **3**, 122–133 (2022).
27. Schneider, C. A., Rasband, W. S. & Eliceiri, K. W. NIH Image to ImageJ: 25 years of image analysis. *Nat. Methods* **9**, 671–675 (2012).
28. Choi, J.-H. *et al.* Single-cell transcriptome profiling of the stepwise progression of head and neck cancer. *Nat. Commun.* **14**, 1055 (2023).
29. Jin, S., Plikus, M. V. & Nie, Q. CellChat for systematic analysis of cell-cell communication from single-cell transcriptomics. *Nat. Protoc.* **20**, 180–219 (2025).
30. Cao, J. *et al.* The single-cell transcriptional landscape of mammalian organogenesis. *Nature* **566**, 496–502 (2019).
31. Qiu, X. *et al.* Reversed graph embedding resolves complex single-cell trajectories. *Nat. Methods* **14**, 979–982 (2017).
32. Liberzon, A. *et al.* Molecular signatures database (MSigDB) 3.0. *Bioinformatics* **27**, 1739–1740 (2011).
33. Smith, E. M., Rubenstein, L. M., Haugen, T. H., Hamsikova, E. & Turek, L. P. Tobacco and alcohol use increases the risk of both HPV-associated and HPV-independent head and neck cancers. *Cancer Causes Control* **21**, 1369–1378 (2010).
34. Demokan, S. & Dalay, N. Role of DNA methylation in head and neck cancer. *Clin.*

Epigenetics **2**, 123–150 (2011).

35. Shrikant Balasaheb, M. Epigenetics: Promising journey so far but ways to go in head neck cancer. *Oral Oncol.* **135**, 106194 (2022).
36. Silva, R. C. M. C., Lopes, M. F. & Travassos, L. H. Distinct T helper cell-mediated antitumor immunity: T helper 2 cells in focus. *Cancer Pathog. Ther.* **1**, 76–86 (2023).
37. Imianowski, C. J., Chen, Q., Workman, C. J. & Vignali, D. A. A. Regulatory T cells in the tumour microenvironment. *Nat. Rev. Cancer* **25**, 703–722 (2025).
38. Campo, M. S. *et al.* HPV-16 E5 down-regulates expression of surface HLA class I and reduces recognition by CD8 T cells. *Virology* **407**, 137–142 (2010).
39. Sen, P., Ganguly, P. & Ganguly, N. Modulation of DNA methylation by human papillomavirus E6 and E7 oncoproteins in cervical cancer. *Oncol. Lett.* **15**, 11–22 (2018).
40. Jiménez-Wences, H., Peralta-Zaragoza, O. & Fernández-Tilapa, G. Human papilloma virus, DNA methylation and microRNA expression in cervical cancer (Review). *Oncol. Rep.* **31**, 2467–2476 (2014).
41. Jiang, M., Li, J., Wei, J., Yang, X. & Wang, W. Advances in neoantigen-based immunotherapy for head and neck squamous cell carcinoma: a comprehensive review. *Front. Oncol.* **15**, 1593048 (2025).
42. McGrail, D. J. *et al.* Multi-omics analysis reveals neoantigen-independent immune cell infiltration in copy-number driven cancers. *Nat. Commun.* **9**, (2018).
43. Gameiro, S. F., Evans, A. M. & Mymryk, J. S. The tumor immune microenvironments of HPV+ and HPV- head and neck cancers. *WIREs Mech. Dis.* **14**, e1539 (2022).
44. Zhang, Y. *et al.* Tumor-specific MHC-II activates CD4+ and CD8+ T cells in head and neck squamous cell carcinoma to boost immunotherapy efficacy. *Cancer Res.* **85**, 3258–3274 (2025).
45. Jenkins, B. H. *et al.* Single cell and spatial analysis of immune-hot and immune-cold tumours identifies fibroblast subtypes associated with distinct immunological niches and positive immunotherapy response. *Mol. Cancer* **24**, 3 (2025).

46. Lander, R. & Petersen, C. P. Wnt, Ptk7, and FGFRL expression gradients control trunk positional identity in planarian regeneration. *Elife* **5**, (2016).
47. Dutton, L. R. *et al.* Fibroblast-derived Gremlin1 localises to epithelial cells at the base of the intestinal crypt. *Oncotarget* **10**, 4630–4639 (2019).
48. Moll, R., Divo, M. & Langbein, L. The human keratins: biology and pathology. *Histochem. Cell Biol.* **129**, 705–733 (2008).
49. Thomas, M. J., Xu, H., Wang, A., Beg, M. A. & Sorci-Thomas, M. G. PCPE2: Expression of multifunctional extracellular glycoprotein associated with diverse cellular functions. *J. Lipid Res.* **65**, 100664 (2024).
50. Micallef, P. *et al.* C1QTNF3 is upregulated during subcutaneous adipose tissue remodeling and stimulates macrophage chemotaxis and M1-like polarization. *Front. Immunol.* **13**, 914956 (2022).
51. Walker, R. C. *et al.* Cancer-associated fibroblasts are associated with neo-adjuvant treatment response in oesophageal adenocarcinoma. *Br. J. Cancer* **133**, 633–647 (2025).
52. Cohen, C., Turner, N. & Moake, J. Human endothelial cells and fibroblasts express and produce the coagulation proteins necessary for thrombin generation. *Research Square* (2021) doi:10.21203/rs.3.rs-784474/v1.
53. Akhmetshina, A. *et al.* Activation of canonical Wnt signalling is required for TGF-β-mediated fibrosis. *Nat. Commun.* **3**, 735 (2012).

Supplemental materials



Supplemental Figure 1. Differentially expressed genes between HPV-positive and HPV-negative tumor associated fibroblasts. A) UMAP of a subset of fibroblasts colored by HPV infection status. B) Feature plot of most significant genes expressed in HPV-negative fibroblasts (left panel) and Violin plots indicating the same set of genes (right panel). C) Feature plot of most significant genes expressed in HPV-positive fibroblasts (left panel) and Violin plots indicating the same set of genes (right panel). Created with BioRender.com (o99u352).

Abbreviations:

CAF, cancer-associated fibroblast

CNA, copy number alteration

CNV, copy number variation

CpG, cytosine–phosphate–guanine

DEG, differentially expressed gene

DMP, differentially methylated position

DNA, deoxyribonucleic acid

ECM, extracellular matrix

FFPE, formalin-fixed paraffin-embedded

FRC, fibroblastic reticular cell

H&E, hematoxylin and eosin

HLA, human leukocyte antigen

HNC, head and neck cancer

HPV, human papillomavirus

IMC, imaging mass cytometry

ISG, interferon-stimulated gene

MHC, major histocompatibility complex

PCA, principal component analysis

scRNA-seq, single-cell RNA sequencing

SMA, smooth muscle actin

T stage, Tumor stage (T1, T2: Early-stage; T3, T4: Advanced-stage)

N stage, Lymph Node stage (N1, N2: Early-stage; N2, N3: Advanced-stage)

TCR, T cell receptor

TH2, T helper type 2

TME, tumor microenvironment

Treg, regulatory T cell

TSS, transcription start site

UMAP, uniform manifold approximation and projection

Supplementary Files

This is a list of supplementary files associated with this preprint. Click to download.

- SupplementalFigure1Fibrobasts.png
- SupplementalTable2TcellDEGclustersmarkers.csv
- SupplementalTable3TcellgeneModules.csv
- SupplementalTable4FibroDEGHPVPosxNeg.csv
- SupplementalTable5metadataIMC.csv
- SupplementalTable6metada450K.csv
- SupplementalTable7antibodies.xlsx
- SupplmentalTable1DMPHPVPosxNeg.csv